Chiral Soliton Lattice Formation in Monoaxial Helimagnet $Yb(Ni_{1-x}Cu_x)_3Al_9$

Takeshi Matsumura[1,2,6,7], Yosuke Kita[1], Koya Kubo[1], Yugo Yoshikawa[1], Shinji Michimura[3], Toshiya Inami[4], Yusuke Kousaka[5,6], Katsuya Inoue[5,6], and Shigeo Ohara[8]

[1]*Department of Quantum Matter, AdSM, Hiroshima University, Higashi-Hiroshima, Hiroshima 739-8530, Japan*
[2]*Institute for Advanced Materials Research, Hiroshima University, Higashi-Hiroshima, Hiroshima 739-8530, Japan*
[3]*Department of Physics, Faculty of Science, Saitama University, Saitama 338-8570, Japan*
[4]*Synchrotron Radiation Research Center, National Institutes for Quantum and Radiological Science and Technology, Sayo, Hyogo 679-5148, Japan*
[5]*Department of Chemistry, Graduate School of Science, Hiroshima University, Higashi-Hiroshima, Hiroshima 739-8526, Japan*
[6]*Chirality Research Center (CResCent), Hiroshima University, Higashi-Hiroshima, Hiroshima 739-8526, Japan*
[7]*Center for Emergent Condensed Matter Physics (ECMP), Hiroshima University, Higashi-Hiroshima, Hiroshima 739-8526, Japan*
[8]*Department of Physical Science and Engineering, Graduate School of Engineering, Nagoya Institute of Technology, Nagoya 466-8555, Japan*

Helical magnetic structures and their responses to external magnetic fields in $Yb(Ni_{1-x}Cu_x)_3Al_9$ with a chiral crystal structure of the space group $R32$ have been investigated by resonant X-ray diffraction. It is shown that the crystal chirality is reflected in the helicity of the magnetic structure by a one-to-one relationship, indicating that an antisymmetric exchange interaction mediated via the conduction electrons exists. When a magnetic field is applied perpendicular to the helical axis (c axis), the second-harmonic peak of $(0, 0, 2q)$ develops with increasing field. The third-harmonic peak of $(0, 0, 3q)$ has also been observed for the x=0.06 sample. This result provides strong evidence for the formation of a chiral magnetic soliton lattice state, a periodic array of chiral twist of spins, which has been suggested by the characteristic magnetization curve. The helical ordering of magnetic octupole moments accompanying the magnetic dipole order has also been detected.

Journal Ref: J. Phys. Soc. Jpn., **86**, 124702 (2017).
http://dx.doi.org/10.7566/JPSJ.86.124702

1. Introduction

Chirality is one of the most fundamental elements of symmetry in nature. It plays an important role in various phenomena ranging from biological functions to the physical properties of inorganic substances.[1)] In magnetic materials lacking the local inversion center for the two-ion exchange interaction, a spiral magnetic order is often stabilized by the antisymmetric Dzyaloshinskii–Moriya (DM) interaction, giving rise to distinct physical properties.[2,3)] The simultaneous appearance of electric polarization with the spiral magnetic order is a typical manifestation of such effects.[4)] In chiral magnetic materials without both inversion and mirror symmetries, a helical magnetic order with a fixed sense of spin rotation can be stabilized. When a magnetic field is applied to such a system, a characteristic arrangement of the topological spin structure is often stabilized through competition between the Zeeman energy and the twisting force from the DM interaction. In cubic B20-type compounds such as MnSi with the space group $P2_13$, for example, the helical spin structure transforms into a hexagonal lattice condensate of magnetic skyrmions.[5–7)] The skyrmion state is a long-range pattern of twisted spin arrangements realized in magnetic fields, which become more stable in two-dimensional configurations in thin films.[8,9)]

In monoaxial chiral helimagnets such as $CrNb_3S_6$ (space group $P6_322$), when a magnetic field is applied perpendicular to the helical axis, the helical ground state transforms into a periodic array of incommensurate chiral spin twists, which separates the ferromagnetically aligned commensurate region.[10–14)] This is a nonlinear order of topological spin structure and is called a chiral soliton lattice (CSL). These materials are expected to provide a new functionality that is operated by tuning the number of skyrmions or solitons in the sample.[15,16)]

In the present paper, we report on the new monoaxial chiral helimagnet system of $Yb(Ni_{1-x}Cu_x)_3Al_9$, in which the CSL state is expected to be realized. The rare-earth compound $YbNi_3Al_9$ has a chiral crystal structure with the space group $R32$ (No. 155), which lacks both space inversion and mirror symmetries.[17,18)] The main block of the crystal structure is shown in Fig. 1 (drawn with VESTA[19)]). The physical properties of $YbNi_3Al_9$ have been studied as those of an Yb-based heavy-fermion compound.[20–25)] Yb ions form a two-dimensional honeycomb lattice in the c plane, which is separated by $c/3$=9.121 Å from the neighbouring Yb layer by five Al and two Ni layers. Since this is much larger than the nearest-neighbor distance of $a/\sqrt{3}$=4.199 Å within a layer, the relation between the two-dimensionality and the heavy-fermion state has also been of interest. The detailed study of this compound from the viewpoint of its chirality started with the discovery of a characteristic magnetization process that is reminiscent of a CSL state.[26)] By substituting Ni with Cu, it was discovered that the $M(H)$ curve behaves similarly to that of $CrNb_3S_6$,[27)] in which the CSL state has clearly been identified.[12–14)]

The exchange interaction in metallic $YbNi_3Al_9$ is considered to be of the Ruderman–Kittel–Kasuya–Yosida (RKKY)

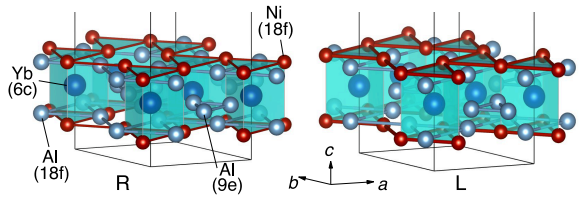

Fig. 1. (Color online) Crystal structure of $YbNi_3Al_9$ with the space group $R32$.[17,18] We call the structure with x=0.3332, y=0.0056, z=0.08517 for the 18f site of Ni the right (R) crystal and its mirror-reflected structure the left (L) crystal. Only the Yb_2(6c)+Al_3(9e)+$2Ni_3$(18f)+$2Al_3$(18f) block layer at the bottom of the unit cell is shown. This block is shifted by $(2/3, 1/3, 1/3)$ and $(1/3, 2/3, 2/3)$. The other Al layers at the 6c and 9d sites are omitted. VESTA was used to draw the figure.[19]

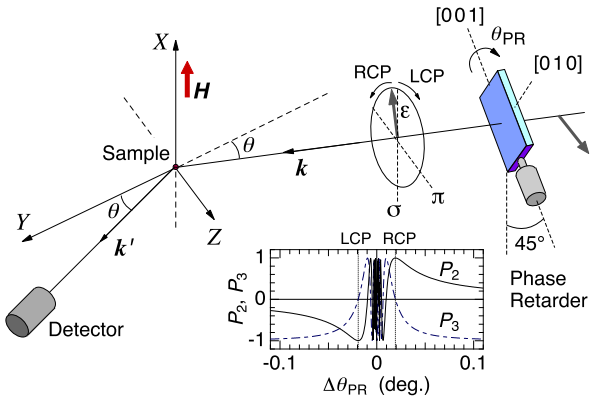

Fig. 2. (Color online) Scattering configuration of the experiment with a phase retarder system inserted in the incident beam. The inset figure shows the $\Delta\theta_{PR} = \theta_{PR} - \theta_B$ dependence of the polarization state using the Stokes parameters P_2 and P_3. The vertical dotted lines represent the positions of LCP and RCP states. The beam is depolarized in the region around $\Delta\theta_{PR} \approx 0$.

type. Since the crystal is chiral, there must be some antisymmetric contribution to the RKKY mechanism in the form of $\boldsymbol{D}_{ij} \cdot \boldsymbol{S}_i \times \boldsymbol{S}_j$, which is generally called the DM interaction.[2,3] Since the microscopic mechanism given by Moriya is based on the superexchange interaction in insulators, the mechanism of the RKKY-type DM interaction is an important subject to be studied. The question is how the crystal chirality is transferred to the spin system of f electrons and conduction electrons.

$YbNi_3Al_9$ is a metallic compound which orders at T_N=3.5 K. It is reported that the magnetic structure of $YbNi_3Al_9$ is helical with propagation vector $(0, 0, \sim 0.8)$ and the moments lying in the c plane. By applying a magnetic field perpendicular to the c axis, the helimagnetic order jumps to a ferromagnetic state at a critical field of H_c=1 kOe.[22,23] By substituting Ni with Cu, both T_N and H_c increase. An anomalous $M(H)$ curve reminiscent of a CSL state is observed for x=0.06.[26] However, the relationship between the crystal chirality and the magnetic helicity, the Cu concentration dependence of the helimagnetic structure, and detailed dependences on the temperature and magnetic field have not yet been studied. The aim of the present study is to clarify these properties experimentally by using resonant X-ray diffraction (RXD).

Experimentally, how to observe a chiral state has long been a subject of interest. Recent progress in the transmission electron microscopy method has made it possible to capture real-space images of skyrmions and CSLs.[5–8,12] It is also of fundamental importance to capture the spatially averaged structure as a Fourier transform of a real-space image by neutron and X-ray diffraction methods. Polarized neutron diffraction is a powerful method for observing the helical magnetic structure and for determining the helicity.[28,29] One drawback of this method is that it is difficult to perform an experiment in magnetic fields because the neutron spin state is affected by the magnetic field. X-ray diffraction, on the other hand, can be used both at zero field and in magnetic fields without any differences. The helicity of a magnetic spiral can be studied by using circularly polarized X-rays.[30–32] By utilizing resonance at an absorption edge of the magnetic element, the scattering cross section is enhanced, making it possible to detect signals from an ordered structure more efficiently.[33] The magnetic skyrmion state in a chiral magnet has been detected by RXD.[34] Furthermore, resonant scattering has sensitivity to higher-order anisotropy (multipole moments) of both magnetic and nonmagnetic nature.[35–37] This sensitivity can sometimes be applied to determine crystal chirality by using a circularly polarized beam.[38–40]

This paper is organized as follows. In Sect. 2, the experimental procedure is described, including the details of the circularly polarized X-ray beam. The experimental results and the analyses are described in Sect. 3. First, in Sect. 3.1, the one-to-one relationship between the crystal chirality and the helimagnetic structure is described. Comparison of the experimental results with the helimagnetic structure model is performed in Sect. 3.2. In Sects. 3.3 and 3.4, the temperature and magnetic field dependences of the helimagnetic order are presented. The resonant nature of the signal is described in Sect. 3.5. We show that the $E2$ resonance involves a signal from a magnetic octupole, which accompanies the helical order of the magnetic dipole. In Sect. 4, we discuss the origin of the octupole moment, the temperature-dependent pitch of the helical structure, and the possibility of the CSL state in $Yb(Ni_{1-x}Cu_x)_3Al_9$. The present study is summarized in Sect. 5.

2. Experiment

Single crystals of $Yb(Ni_{1-x}Cu_x)_3Al_9$ were prepared by an Al-flux method following the procedure described in the literature.[26] The starting composition x' of Cu sealed in a quartz ampoule was set to five times the target composition x. The actual Cu concentration x in the obtained crystal was verified by electron probe microanalysis and was confirmed to follow the relation $x \sim 0.2x'$, as reported previously.[26] We also verified the sample quality by magnetic susceptibility, magnetization, and electrical resistivity measurements and obtained consistent results with those reported in the literature.[22,26]

RXD experiments were performed at BL22XU at SPring-8. The c-plane surfaces of the samples were mirror-polished, and the samples were mounted in a vertical-field 8 T superconducting cryomagnet equipped with a ^{3}He cryostat insert so that the c axis was perpendicular to the magnetic field and coincided with the scattering vector $\boldsymbol{k}' - \boldsymbol{k} \parallel \hat{Z}$. The scattering geometry is shown in Fig. 2. The incident X-ray energy was tuned to the L_3 edge of Yb.

We used a diamond phase retarder system to tune the horizontally polarized incident beam to a circularly polarized

state.[41] By rotating the angle of the diamond phase plate θ_{PR} about the 220 Bragg angle θ_B, where the scattering plane is tilted by 45°, a phase difference arises between the σ and π components of the transmitted beam. The phase difference is approximately proportional to $1/(\theta_{PR} - \theta_B)$. This allows us to tune the incident linear polarization to right-handed circular polarization (RCP) and left-handed circular polarization (LCP) by changing $\Delta\theta_{PR} = \theta_{PR} - \theta_B$. The polarization state of the incident beam as a function of $\Delta\theta_{PR}$ is shown in Fig. 2 using the Stokes parameters P_2 (+1 for RCP and −1 for LCP) and P_3 (+1 for σ and −1 for π linear polarization).[42] In the horizontal scattering plane configuration in the present experiment, the incident linear polarization is π when $\Delta\theta_{PR}$ is large. P_1 (+1 for 45° and −1 for −45° linear polarization) is zero in the present setup.

We define RCP as $\varepsilon_R = (\varepsilon_\sigma + i\varepsilon_\pi)e^{i(\boldsymbol{k}\cdot\boldsymbol{r}-\omega t)}$ and LCP as $\varepsilon_L = (\varepsilon_\sigma - i\varepsilon_\pi)e^{i(\boldsymbol{k}\cdot\boldsymbol{r}-\omega t)}$. We verified the helicity of the incident photon after transmitting the phase retarder by measuring the resonant scattering intensity of a forbidden reflection from $P6_122$-type $CsCuCl_3$, where the intensity ratio between RCP and LCP X-rays depends on the reflection index and is exactly determined by the $P6_122$ space group.[38]

The crystal chirality of the sample was determined by using a laboratory-based X-ray diffraction system (Bruker APEX-II) and it was also verified in the RXD experiment at the beamline. In the former method, using a Mo K_α X-ray beam, the Flack parameter was deduced by analyzing the intensities of many reflections, which resulted in either 0 (R) or 1 (L). Our definition of the crystal chirality is shown in Fig. 1. Then, R and L samples were selected for each Cu concentration for use with the RXD experiment. At the beamline, the energy dependences of the $(1, 1, 24)$ and $(\bar{1}, \bar{1}, 24)$ fundamental Bragg peak intensities were measured around the absorption edge of Yb, which is shown in Fig. A·1 in Appendix A. The spectrum exhibited a contrasting energy dependence at the edge depending on the chirality of the crystal. It was consistent with the calculated spectrum assuming the predetermined crystal chirality, confirming that the irradiated spot of the sample in the RXD experiment has exactly the same chirality as that determined in the laboratory X-ray diffraction. It was also confirmed at the beamline that the $(1, 0, 3n + 1)$ reflections are allowed and the $(1, 0, 3n)$ and $(1, 0, 3n - 1)$ reflections are forbidden as shown in Fig. A·2. This fact guarantees the threefold symmetry of the sample about the c axis. If the forbidden reflections were observed, it would have meant that the [1 1 0] axis was mixed with the a axis due to the stacking fault of 60°.

3. Results and Analysis

3.1 *Crystal chirality and the helical magnetic structure*

First, we demonstrate that the crystal chirality and the helicity of the helical magnetic structure have a one-to-one relationship. A typical example is shown in Fig. 3 for the R and L crystals with x=0.06. The reciprocal scans along (0, 0, L) around the $(0, 0, 27)$ fundamental Bragg peak using RCP and LCP X-rays exhibit opposite behavior for the R and L crystals as well as those for the $(0, 0, 27 - q)$ and $(0, 0, 27 + q)$ peaks. In the R(L) crystal at $(0, 0, 27 - q)$, the intensity is strong (weak) for LCP and weak (strong) for RCP. This relation is reversed at $(0, 0, 27+q)$. The X-ray energy of 8.944 keV corresponds to the $E1$ ($2p \leftrightarrow 5d$) resonance. The energy dependence of the intensity demonstrating the resonance feature will be shown later. In Fig. 3, the peaks are observed at an incommensurate wave vector of q=0.445 for the L crystal and q=0.425 for the R crystal. This difference in the q value is due to the difference in the sample quality, i.e., a slight difference in the Cu concentration, and is unrelated to the chirality.

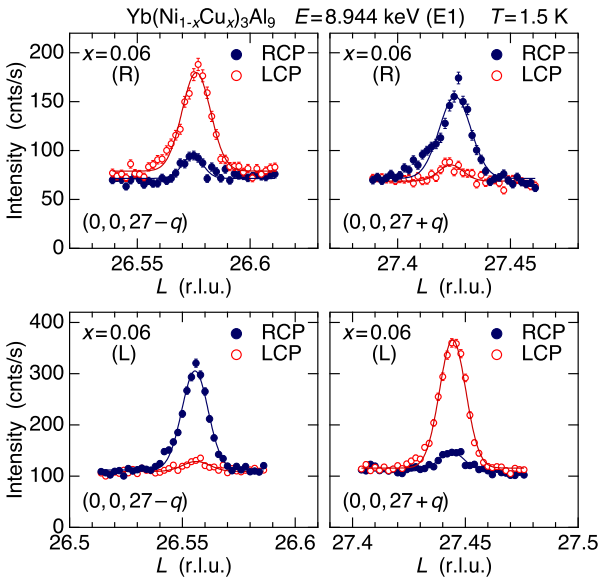

Fig. 3. (Color online) Reciprocal space scan along $(0, 0, L)$ around the $(0, 0, 27)$ fundamental peak for the x=0.06 sample with right and left chirality using RCP and LCP X-rays. Solid lines are the fits with Gaussian functions.

More detailed information can be extracted from the $\Delta\theta_{PR}$ scans, which are shown in Fig. 4. This figure shows not only the intensity relations for the RCP and LCP X-rays at $(0, 0, 27 \pm q)$ but also the overall feature of the incident polarization dependence as a function of $\Delta\theta_{PR}$. The incident polarization state varies with $\Delta\theta_{PR}$ as shown in the inset of Fig. 2. We again observe from this measurement that the crystal chirality and the helicity of the magnetic structure have a one-to-one relationship. In addition, the relationship does not change with the Cu concentration between x=0 and x=0.06. The solid lines in the figures represent the calculated curves expected from the helical magnetic structure with the moments lying in the c plane and propagating along the c axis. Next, we describe the analysis of the above experimental results.

3.2 *Magnetic structure*

There are two Yb atoms for the 6c site of the $R32$ space group: Yb-1 at $\boldsymbol{d}_1 = (0, 0, z)$ and Yb-2 at $\boldsymbol{d}_2 = (0, 0, \bar{z})$, where z=0.167∼ 1/6. In the present single-$\boldsymbol{q}$ magnetic structure, the magnetic moments $\boldsymbol{\mu}_{1,j}$ and $\boldsymbol{\mu}_{2,j}$ of Yb-1 and Yb-2, respectively, on the jth lattice point at $\boldsymbol{r}_j = (n_1, n_2, n_3)$, $(n_1 + 2/3, n_2 + 1/3, n_3 + 1/3)$, and $(n_1 + 1/3, n_2 + 2/3, n_3 + 2/3)$, where n_1, n_2, and n_3 are integers, are generally expressed as

$$\boldsymbol{\mu}_{1,j} = \boldsymbol{m}_1 e^{i\boldsymbol{q}\cdot\boldsymbol{r}_j} + \boldsymbol{m}_1^* e^{-i\boldsymbol{q}\cdot\boldsymbol{r}_j}, \quad (1a)$$

$$\boldsymbol{\mu}_{2,j} = \boldsymbol{m}_2 e^{i\boldsymbol{q}\cdot\boldsymbol{r}_j} + \boldsymbol{m}_2^* e^{-i\boldsymbol{q}\cdot\boldsymbol{r}_j}, \quad (1b)$$

where $\boldsymbol{m}_1$ and $\boldsymbol{m}_2$ are the magnetic amplitude vectors of Yb-1 and Yb-2, respectively. In the present case of $Yb(Ni_{1-x}Cu_x)_3Al_9$, since the moments are expected to be ordered within the c plane, $\boldsymbol{m}_1$ and $\boldsymbol{m}_2$ can generally be written

Table I. Relation among the phase φ, Fourier component $\boldsymbol{m}$, scattering vector $\boldsymbol{Q}$, magnetic structure factor $\boldsymbol{Z}^{(1)}_{\rm dip}$, sign of C_2, and crystal chirality.

φ	$\boldsymbol{m}$	$\boldsymbol{Q}$	$\boldsymbol{Z}^{(1)}_{\rm dip}$	C_2	Crsytal
$\pi/2$	$\hat{\boldsymbol{x}}+i\hat{\boldsymbol{y}}$	$(0,0,3n\pm q)$	$(1,\pm i,0)$	$\pm$	R
$-\pi/2$	$\hat{\boldsymbol{x}}-i\hat{\boldsymbol{y}}$	$(0,0,3n\pm q)$	$(1,\mp i,0)$	$\mp$	L

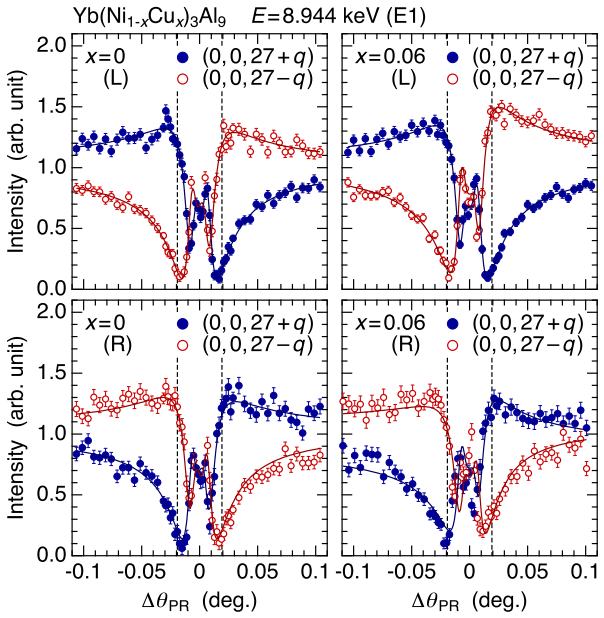

Fig. 4. (Color online) Incident polarization ($\Delta\theta_{\rm PR}$) dependence of the intensities at $(0,0,27\pm q)$ for x=0 and x=0.06 crystals with right and left chirality. The background has been subtracted. Solid lines are the calculations described in the text.

as $\boldsymbol{m}_1 = m_1(\hat{\boldsymbol{x}}+e^{i\varphi}\hat{\boldsymbol{y}})$ and $\boldsymbol{m}_2 = m_2 e^{i\delta}(\hat{\boldsymbol{x}}+e^{i\varphi}\hat{\boldsymbol{y}})$, where $\hat{\boldsymbol{x}}$ and $\hat{\boldsymbol{y}}$ represent the unit vectors along the x and y axis, respectively, which are taken perpendicular to the c (z) axis. The irreducible representation of the $\boldsymbol{m}$-vector for $\boldsymbol{q}=(0,0,q)$, where q is an incommensurate value, is written as $\hat{\boldsymbol{x}}\pm i\hat{\boldsymbol{y}}$. Therefore, φ is either $\pi/2$ or $-\pi/2$. The phase difference between $\boldsymbol{\mu}_{1,j}$ and $\boldsymbol{\mu}_{2,j}$ is represented by δ. The above expression for the magnetic structure can be reduced to

$$\boldsymbol{\mu}_{1,j} = m_1\{\hat{\boldsymbol{x}}\cos\boldsymbol{q}\cdot\boldsymbol{r}_j + \hat{\boldsymbol{y}}\cos(\boldsymbol{q}\cdot\boldsymbol{r}_j+\varphi)\}, \tag{2a}$$

$$\boldsymbol{\mu}_{2,j} = m_2\{\hat{\boldsymbol{x}}\cos(\boldsymbol{q}\cdot\boldsymbol{r}_j+\delta) + \hat{\boldsymbol{y}}\cos(\boldsymbol{q}\cdot\boldsymbol{r}_j+\varphi+\delta)\}. \tag{2b}$$

Since $\varphi=\pm\pi/2$, the above expression describes a perfect helical structure with helicity ±1 in which the adjacent Yb-1 (or Yb-2) moments on the neighboring layers along the c axis make a fixed angle of $2\pi q/3$. On the other hand, the angle between the Yb-1 and Yb-2 moments within a layer, the former at $(0,0,z)$ and the latter at $(2/3,1/3,1/3)+(0,0,\bar{z})$ in Fig. 1, is described by the parameter δ. This angle is reported to be 20.5° for x=0.[43] Note that our experimental results presented in this paper, which were collected only along the $(0,0,L)$ line, are not sufficiently sensitive to determine the δ value.

The $E1$ resonant scattering amplitude from the magnetic dipole order is proportional to $i(\boldsymbol{\varepsilon}'\times\boldsymbol{\varepsilon})\cdot\boldsymbol{Z}^{(1)}_{\rm dip}$,[33,35] where

$$\boldsymbol{Z}^{(1)}_{\rm dip} = \sum_{j,d}\boldsymbol{\mu}_{j,d}e^{-i\boldsymbol{Q}\cdot(\boldsymbol{r}_j+\boldsymbol{d})} \tag{3}$$

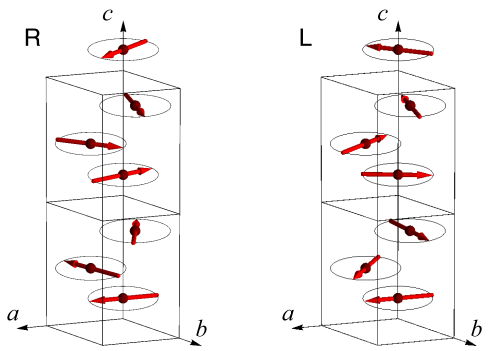

Fig. 5. (Color online) Magnetic structure of $Yb(Ni_{1-x}Cu_x)_3Al_9$ for x=0.06. Only the moments on the Yb-1 sites are shown.

represents the magnetic structure factor at $\boldsymbol{Q}=\boldsymbol{k}'-\boldsymbol{k}$. At $\boldsymbol{Q}=(0,0,3n\pm q)$, $\boldsymbol{Z}^{(1)}_{\rm dip}=(1,\pm i,0)$ when $\varphi=\pi/2$, and $\boldsymbol{Z}^{(1)}_{\rm dip}=(1,\mp i,0)$ when $\varphi=-\pi/2$. The scattering amplitude matrix, as defined in Appendix B, for the magnetic structure factor $(1,\pm i,0)$ is expressed as

$$\hat{F}_{E1} = \begin{pmatrix} 0 & i\cos\theta \\ -i\cos\theta & \mp\sin 2\theta \end{pmatrix}. \tag{4}$$

Then, following the method described in Appendix B, we can calculate the coefficients C_n (n=0–3) defined in Eq. (B·5), which express the scattering cross sections. The parameters C_2/C_0 and C_3/C_0, as normalized by the total cross section C_0, correspond to the intensity terms proportional to P_2 and P_3, respectively. When $C_2>0$, the intensity is stronger for the RCP ($\Delta\theta_{\rm PR}>0$). For $\boldsymbol{Q}=(0,0,27\pm q)$, when $\varphi=\pi/2$, $C_2/C_0=\pm0.71$ and $C_3/C_0=-0.47$ are obtained. The observed intensity is a superposition of the P_2 and P_3 terms. The experimental data in Fig. 4 show that at $\boldsymbol{Q}=(0,0,27+q)$ $C_2>0$ in the R-crystal and $C_2<0$ in the L-crystal. This means that $\varphi=\pi/2$ ($\boldsymbol{m}=\hat{\boldsymbol{x}}+i\hat{\boldsymbol{y}}$) in the R-crystal and $\varphi=-\pi/2$ ($\boldsymbol{m}=\hat{\boldsymbol{x}}-i\hat{\boldsymbol{y}}$) in the L-crystal. These relations are summarized in Table I. The magnetic structure is shown in Fig. 5 for x=0.06. The Yb-2 moment is not shown because the relative angle with the Yb-1 moment is unknown. The solid lines in Fig. 4 are the calculations using the C_2/C_0 and C_3/C_0 values calculated above, which agree well with the experimental data.

3.3 *Temperature dependence*

Figure 6 shows the $(0,0,L)$ peak profile for x=0 (L) and x=0.06 (L) samples. With increasing T, the intensity decreases and vanishes at $T_{\rm N}$, indicating that the resonant signal is of magnetic origin. In addition, the peak position shifts with the temperature. It is also noteworthy that the direction of the peak shift for x=0.06 is opposite to that for x=0. It depends on the Cu concentration x but does not depend on the chirality of the crystal.

The parameters obtained from the $(0,0,L)$ scans are summarized in Fig. 7. For x=0, the q value decreases with decreasing T and saturates at ~ 0.818 at the lowest temperature, indicating that the helical structure is incommensurate with the lattice. The T dependence of the q value becomes weak for x=0.02. Surprisingly, at x=0.04, the direction of the T dependence is reversed and the q value increases with decreas-

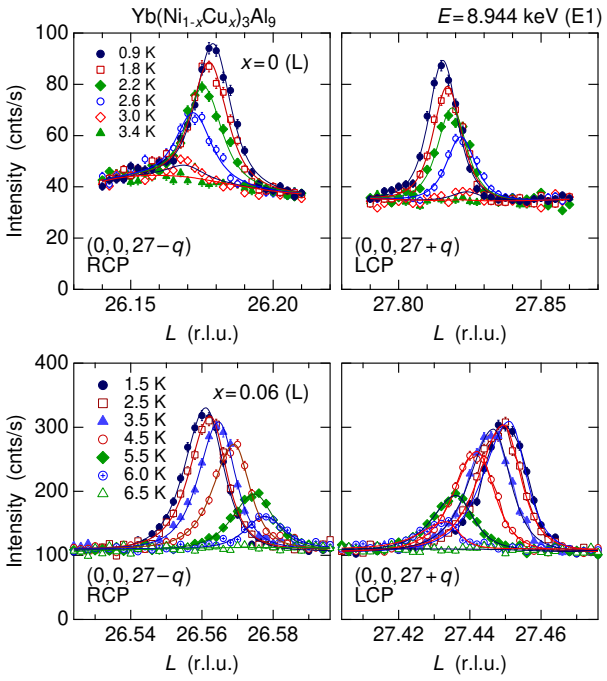

Fig. 6. (Color online) Temperature dependence of the peak profile for x=0 (L) and x=0.06 (L).

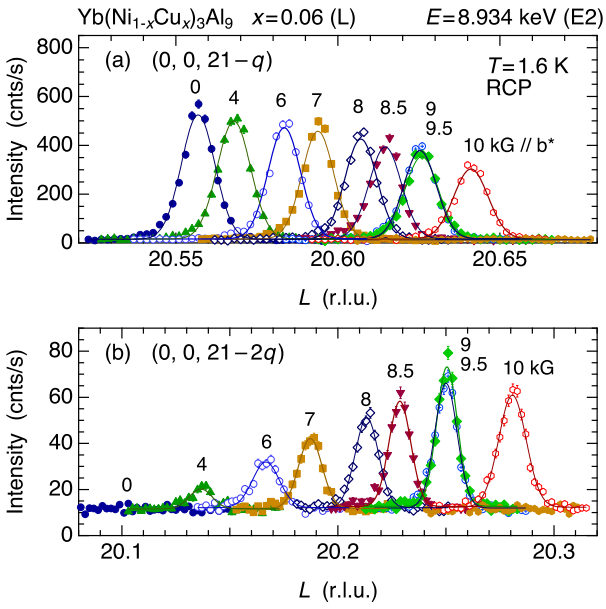

Fig. 8. (Color online) Magnetic field dependence of the peak profile for x=0.06 measured with the RCP photon at the $E2$ resonance energy. (a) First harmonic peak at $(0, 0, 21 - q)$. (b) Second harmonic peak at $(0, 0, 21 - 2q)$. The field is applied perpendicular to the c axis ($\parallel b^*$).

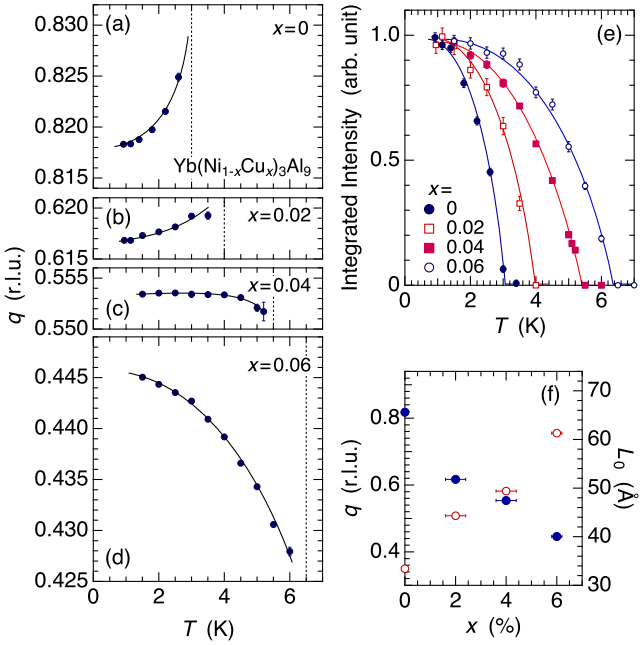

Fig. 7. (Color online) (a)–(d) Temperature dependence of the q value of the propagation vector. The vertical dashed line represents T_N. (e) Temperature dependence of the normalized intensity. (f) Cu concentration dependence of the q value (closed circles) and the pitch $L_0 = c/q$ (open circles) at the lowest temperature.

ing T. At x=0.06, the T dependence becomes strong again. It seems that the direction of the shift in the q value is reversed at around x=0.03, where $q \sim 0.6$.

Figure 7(e) shows the T dependence of the integrated intensity for all the Cu concentrations. T_N increases roughly proportionally to x, which is consistent with the literature.[26,44]

In addition, the shift of the q value mentioned above, regardless of its direction, is almost proportional to the intensity, which reflects the development of the ordered moment. This suggests that the q-shift is associated with the magnitude of the ordered moment. In Fig. 7(f), we show the x dependence of the q value and the pitch $L_0 = c/q$ at the lowest temperature. L_0 should be compared with the interlayer distance of $c/3 \sim 9.1$ Å. The angle between the moments on neighboring layers is calculated as $2\pi q/3$, i.e., 98.2, 74.0, 66.4, and 53.4° for x=0, 0.02, 0.04, and 0.06, respectively, at the lowest temperature.

3.4 *Magnetic field dependence*

Figure 8(a) shows the magnetic field dependence of the peak profile of $(0, 0, 21 - q)$ for the x=0.06 (L) sample, measured at the $E2$ ($2p \leftrightarrow 4f$) resonance energy of 8.934 keV, where the signal-to-noise ratio was much higher than that at the $E1$ resonance. The energy dependence of the resonant signal will be shown later. We used the RCP photon with stronger scattering intensity for the L-crystal than the LCP photon. The result for the second-harmonic peak measured at $(0, 0, 21-2q)$ is shown in Fig. 8(b). With increasing H, the peak position shifts to the fundamental Bragg peak at $(0, 0, 21)$ and the intensity of the first-harmonic (q) peak gradually decreases. On the other hand, the intensity of the second-harmonic ($2q$) peak, which does not exist at zero field, gradually increases with increasing H.

The magnetic field dependence of the q values and the integrated intensities of the q and $2q$ peaks for x=0.02, 0.04, and 0.06 are summarized in Fig. 9. Although all these measurements were performed using the L-crystals, the results do not depend on the crystal chirality. For all the Cu concentrations, it is commonly observed that the q value decreases with increasing H, which becomes more rapid at higher fields on approaching the critical field H_c. Note that q does not decrease

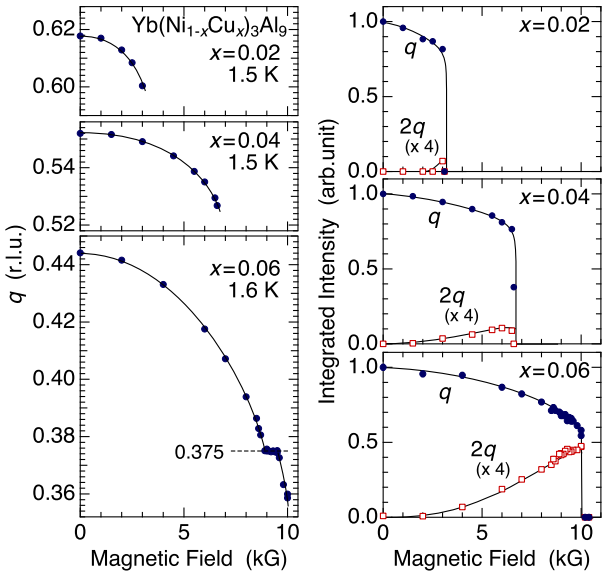

Fig. 9. (Color online) Magnetic field dependence of the q values (left column) and the integrated intensities (right column). The integrated intensities for the $2q$ peak are multiplied by four.

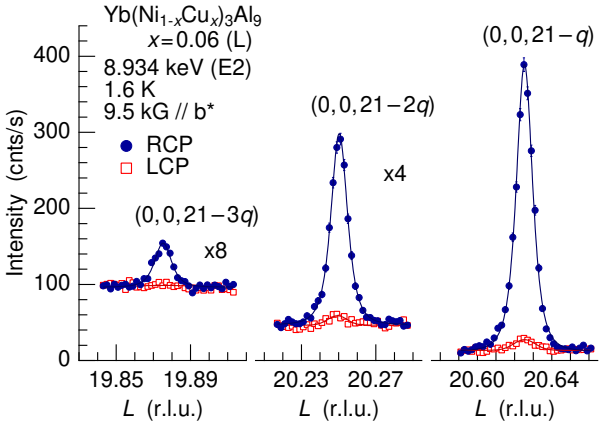

Fig. 10. (Color online) L-scan profiles for the higher-harmonic peaks of $(0, 0, 21 - nq)$ $(n = 1, 2, 3)$ observed at 9.5 kG for x=0.06 (L).

continuously to zero but jumps to zero at H_c. The integrated intensity of the q peak gradually decreases with increasing H and also jumps to zero at H_c. These results show that the transition at H_c is of first-order. It is also a common characteristic that the $2q$ peak is gradually induced with increasing H. This is observed even for the x=0.02 sample with $\mu_0 H_c$=3 kG.

Another noteworthy result is the locking-in behavior of the helical magnetic propagation vector at q=0.375=3/8 between 9 and 9.5 kG for x=0.06. As observed in Fig. 8, the peak position does not change in this field region. The $2q$ peak is also fixed at $2q$=3/4. This result shows that some coupling exists between the helimagnetic structure and the lattice, although the magnetic anisotropy in the c plane is considered to be very small. There is no hysteresis in this behavior, which can be observed in both field-increasing and -decreasing processes. It is also interesting that the lock-in does not seem to exist at q=3/7=0.4286 at around 5 kG. This suggests that the lock-in is more associated with the $2q$ peak, which develops at high fields, than the q peak existing from zero field to high fields.

At 9.5 kG, slightly below the critical field of 10 kG for the ferromagnetic state in the x=0.06 (L) sample, we searched for more higher-order harmonics and successfully detected the third-harmonic peak. The result is shown in Fig. 10. For all the harmonics, the scattering intensity for the RCP photon is stronger than that for the LCP photon, indicating that the magnetic helicity of the modulated structure giving the higher harmonic is the same as that of the original helical structure of the first harmonic. The fourth-harmonic peak was too weak to be recognized above the background. The integrated intensities of the $2q$ and $3q$ peaks are approximately 6 and 50 times weaker, respectively, than that of the q peak.

The H dependence of the q value directly shows that the pitch of the helimagnetic structure increases with increasing H. In addition, the appearance of the higher-harmonic peaks shows that some additional structure is superimposed with increasing H. It is noteworthy that the H dependence of the q and $2q$ peak intensities shown in Fig. 9 is very similar to the calculation for the chiral sine-Gordon model (see Fig. 25 of Ref. 10 or Fig. 13 of Ref. 11). This result, as well as the H dependence of q which is associated with L_0/L_{CSL} (Fig. 13 of Ref. 10 or Fig. 38 of Ref. 11), strongly indicates that a CSL state is formed in $Yb(Ni_{1-x}Cu_x)_3Al_9$, especially for x=0.06.

3.5 *Energy spectrum*

Figure 11 shows the energy dependence of the $(0, 0, 27 - q)$ peak at 0 kG and the $(0, 0, 27 - 2q)$ peak at 9 kG measured for x=0.06 (L). The two resonant peaks are well separated at 8.934 and 8.944 keV. The former can be assigned to the $E2$ resonance ($2p \leftrightarrow 4f$) peak and the latter to the $E1$ resonance ($2p \leftrightarrow 5d$) peak. In the tail on the lower-energy side of the $(0, 0, 27-q)$ peak we can see weak nonresonant magnetic scattering. The energy dependence for the second-harmonic peak also exhibits resonances at the $E2$ and $E1$ energies. No nonresonant signal was observed. This shows that the resonant signal of the second harmonic can be ascribed to the helical magnetic order itself and not to a possible lattice deformation induced by the magnetic order. These features of the energy dependence were commonly observed for other Cu concentrations.

3.6 *Contribution of magnetic octupole to the E2 resonance*

Figure 12 shows the $\Delta\theta_{PR}$ dependence of the $(0, 0, 27 - q)$ peak intensity at zero field and the $(0, 0, 27 - 2q)$ peak intensity at 9.9 kG at the $E2$ resonance energy. We notice that the $\Delta\theta_{PR}$ dependence appears to be different from that in Fig. 4 for the $E1$ resonance. The $E2$ intensity is strongly enhanced when $\Delta\theta_{PR}$ is tuned to the LCP or RCP position. The result that the two $\Delta\theta_{PR}$ dependences are very similar shows that the structure factors for the q and $2q$ peaks are almost the same. By fitting these $\Delta\theta_{PR}$ dependences using Eq. (B·5), we obtain three parameters, C_0, C_2, and C_3. The parameters obtained for various $\boldsymbol{Q}$ vectors for the first harmonic peak from $(0, 0, 6 \pm q)$ to $(0, 0, 30 \pm q)$ for the x=0.06 (R) sample are shown in Fig. 13. The parameters C_2 and C_3 are normalized by C_0. Note that the sign of C_2 in Fig. 13 is opposite to the one deduced from Fig. 12 because the crystal chirality is opposite. With respect to the $E1$ resonance, the Q-dependence data in Fig. 13(a) can be well reproduced by the scattering amplitude

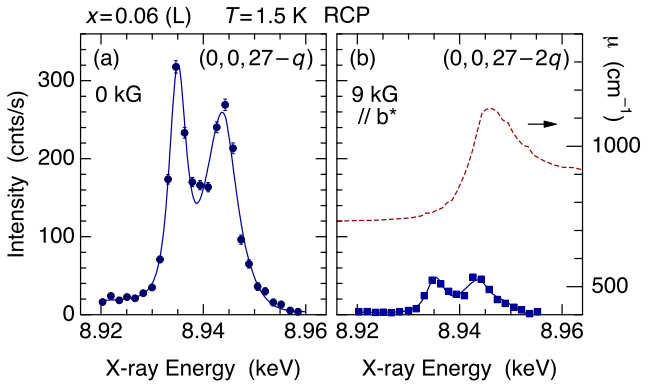

Fig. 11. (Color online) Energy dependence of (a) the $(0, 0, 27 - q)$ peak intensity at zero field and (b) the $(0, 0, 27 - 2q)$ peak intensity at 9 kG for x=0.06 (L) measured with RCP incident photons after background subtraction and absorption correction. The absorption coefficient obtained from the fluorescence spectrum is shown in the right panel.

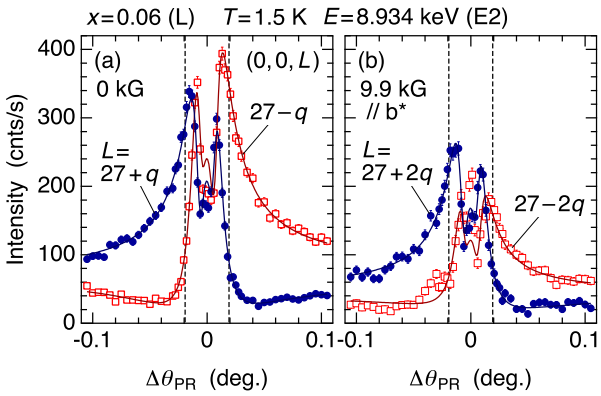

Fig. 12. (Color online) $\Delta\theta_{\rm PR}$ dependence of the $E2$ resonance intensity for (a) $(0, 0, 27 \pm q)$ at 0 kG and (b) $(0, 0, 27 \pm 2q)$ at 9.9 kG. The vertical dashed lines represent the positions of the LCP and RCP states. Solid lines are the fits using Eq. (B·5).

of the magnetic dipole, $i(\boldsymbol{\varepsilon}' \times \boldsymbol{\varepsilon}) \cdot \boldsymbol{Z}^{(1)}_{\rm dip}$, as explained in §3.2. The calculated Q-dependences of the parameters are shown by the lines in Fig. 13(a).

The problem is that the results of the $E2$ resonance in Figs. 12(a) and 13(b) cannot be reproduced by the scattering from the magnetic dipole moment. Using Eq. (B·10), the $E2$ scattering-amplitude matrix for the magnetic dipole with the structure factor $(1, \pm i, 0)$ is expressed as

$$\hat{F}_{E2} = \begin{pmatrix} \mp \sin 2\theta & i \cos 3\theta \\ -i \cos 3\theta & \mp 2 \sin 4\theta \end{pmatrix} . \tag{5}$$

For $\boldsymbol{Q} = (0, 0, 27 \pm q)$, when $\varphi = \pi/2$ for the R-crystal in the present case, $C_2/C_0 = \mp 0.79$ and $C_3/C_0 = 0.51$ are obtained by calculation. However, the sign of C_2 is opposite to the experimental result. In addition, since the $\cos 3\theta$ in $\hat{F}_{\pi\sigma'}$ and $\hat{F}_{\sigma\pi'}$ changes sign at $\theta = \pi/6$, C_2 in Fig. 13(b) should change sign around L=20, which clearly disagrees with the experimental result.[45] Therefore, we cannot explain the $E2$ resonance by only the scattering from the magnetic dipole.

The Q-dependence of C_2 and C_3 for $E2$ can be reproduced by considering the scattering from the magnetic octupole. We use the following model. First, the structure factor of the mag-

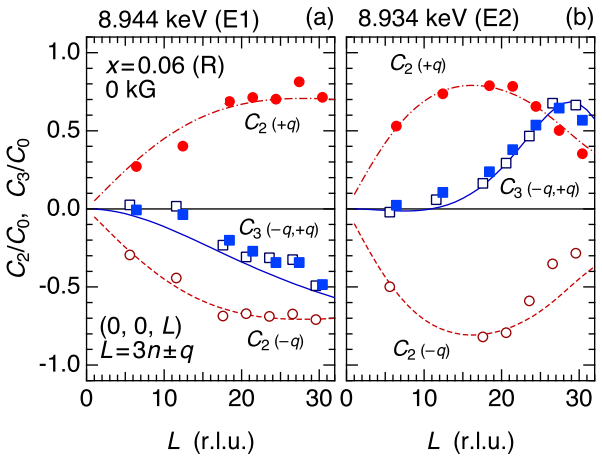

Fig. 13. (Color online) L $(= 3n \pm q)$ dependence of the parameters C_2/C_0 and C_3/C_0 at zero field obtained from the $\Delta\theta_{\rm PR}$ scans for the x=0.06 (R) sample at (a) $E1$ resonance and (b) $E2$ resonance. Solid, dashed, and dot-dashed curves represent the calculations of C_3/C_0 $(L = 3n \pm q)$, C_2/C_0 $(L = 3n - q)$, and C_2/C_0 $(L = 3n + q)$, respectively, for (a) $E1$ resonant scattering from helimagnetic dipole order and (b) $E2$ resonant scattering from helimagnetic dipole and octupole order.

netic dipole (rank-1) for $\boldsymbol{Q} = (0, 0, 3n \pm q)$ for the R-crystal is represented by

$$\boldsymbol{Z}^{(1)}_{\rm dip} = (1, \pm i, 0) . \tag{6}$$

Second, we take into account the $T^{\alpha}_{x,y,z}$ (T_{1u}) and $T^{\beta}_{x,y,z}$ (T_{2u}) magnetic octupole (rank-3). The structure factors of these moments, which are compatible with the helical magnetic dipole order, should be written as

$$\boldsymbol{Z}^{(3)}_{\alpha} = \sqrt{3} A e^{i\phi} (1, \pm i, 0) , \tag{7a}$$

$$\boldsymbol{Z}^{(3)}_{\beta} = \sqrt{5} A e^{i\phi} (1, \mp i, 0) , \tag{7b}$$

where A and ϕ represent the relative amplitude and phase, respectively, of the octupolar structure factor with respect to those of $\boldsymbol{Z}^{(1)}_{\rm dip}$. By putting $A = 0.46$ and $\phi = -0.79\pi$, the data are well explained as shown by the calculated curves in Fig. 13(b). The $\Delta\theta_{\rm PR}$ dependence in Fig. 12(a) can also be reproduced by using these parameters.

The detailed relationship of the coefficients between Eqs. (7a) and (7b) originates from the irreducible representation of the order parameter in the D_3 point group.[46] Although we use the cubic coordinates for the intensity calculation, we should analyze the order parameter using the hexagonal coordinates. The in-plane dipole moments, J_x and J_y, for example, belong to the two-dimensional E_u representation in the D_3 point group. The octupole moments with the E_u representation, on the other hand, are expressed as linear combinations of T^{α} and T^{β}. They are written as $T^{\gamma}_x = (-\sqrt{3}T^{\alpha}_x - \sqrt{5}T^{\beta}_x)$ and $T^{\gamma}_y = (-\sqrt{3}T^{\alpha}_y + \sqrt{5}T^{\beta}_y)$. Therefore, the ordered structure of the octupole moments given by Eqs. (7a) and (7b) is equivalent to the helical octupole ordering expressed by $T^{\gamma}_x + iT^{\gamma}_y$, which has the same symmetry as the helical magnetic dipole order expressed by $J_x + iJ_y$. Although the opposite sign of $\boldsymbol{Z}^{(3)}_{\beta,y}$ in Eq. (7b) is a rather tricky result, it is not surprising.

Other representations are given by $T^{\delta}_x = (\sqrt{5}T^{\alpha}_x - \sqrt{3}T^{\beta}_x)$ (A_{2u}) and $T^{\delta}_y = (\sqrt{5}T^{\alpha}_y + \sqrt{3}T^{\beta}_y)$ (A_{1u}). T_{xyz} and T^{β}_z also constitute another E_u representation in the D_3 group. Although

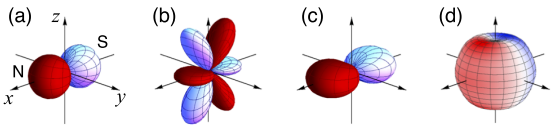

Fig. 14. (Color online) Magnetic charge distributions representing (a) a magnetic dipole J_x, (b) a magnetic octupole $-T_x^\gamma$, (c) the superposition of J_x and $-T_x^\gamma$. (d) Charge and magnetic charge density of the $|7/2, \pm 1/2\rangle$ state of Yb^{3+}, possessing a magnetic dipole moment $\langle J_x \rangle$.[47)]

these moments generally need to be included, the data were successfully explained without taking them into account.

4. Discussion

4.1 *Helical order of octupole moments*

The ground multiplet of $J = 7/2$ for Yb^{3+} splits into four Kramers doublets in the crystalline electric field of $YbNi_3Al_9$, represented by the point group D_3. Since the magnetic moments preferentially lie in the c plane, the crystal field ground state is likely to be composed mainly of $|\frac{7}{2}, \pm\frac{1}{2}\rangle$, which is isotropic in the c plane. In this two-dimensional space of $|\frac{7}{2}, \pm\frac{1}{2}\rangle$, the x-component matrices of $\hat{J}_x$ (E_u dipole) and $\hat{T}_x^\gamma$ [$x(5z^2 - r^2)$-type, E_u octupole] are expressed in the same form as

$$\hat{J}_x = 2\begin{pmatrix} 0 & 1 \\ 1 & 0 \end{pmatrix}, \quad \hat{T}_x^\gamma = -15\sqrt{\frac{3}{2}}\begin{pmatrix} 0 & 1 \\ 1 & 0 \end{pmatrix}. \tag{8}$$

Therefore, when a magnetic dipole moment $\langle J_x \rangle$ is induced, the $\langle T_x^\gamma \rangle$ octupole arises simultaneously. When a helical magnetic dipole order of $\langle J_x + iJ_y \rangle$ occurs, the helical magnetic octupole order of $\langle T_x^\gamma + iT_y^\gamma \rangle$ with the same helicity also arises. The matrix elements of the T_{xyz} and T_z^β octupoles (E_u), T_x^δ (A_{2u}), and T_y^δ (A_{1u}) all vanish in the $|\frac{7}{2}, \pm\frac{1}{2}\rangle$ space. This is the reason we did not need to include these moments in the analysis in §3.6. Also, there is no degree of freedom for the quadrupole (rank-2) moments, which guarantees the reasoning that the orbital contribution is not included in the second-harmonic signal.

The T^γ-type magnetic octupole reflects an aspherical charge distribution of the $|\frac{7}{2}, \pm\frac{1}{2}\rangle$ states. Figure 14 shows schematics of the magnetic charge distributions.[47)] The superposition of the J_x-dipole and the T^γ-octupole, shown in Figs. 14(a) and 14(b), respectively, results in the magnetic charge distribution shown in Fig. 14(c). We see a lower magnetic moment density along the c (z) axis, which is associated with the lower charge density of the $|\frac{7}{2}, \pm\frac{1}{2}\rangle$ state along the c axis as shown in Fig. 14(d).

At the present stage, it is not clear whether the octupole moments affect any physical property in $Yb(Ni_{1-x}Cu_x)_3Al_9$. It should be remarked, however, that the strength of the interionic multipolar interaction is rank-independent in the RKKY mechanism.[48,49)] As a result, the higher-rank multipoles play important roles in the physical properties and can equally be a primary order parameter, as is typically realized in the cubic $Ce_xLa_{1-x}B_6$ system, in which the dipole, quadrupole, and octupole moments are active as independent degrees of freedom.[50,51)] In $Yb(Ni_{1-x}Cu_x)_3Al_9$, by contrast, the active moments in the doublet ground state are (J_x, J_y) or (T_x^γ, T_y^γ), which both belong to the E_u representation and are not independent. The issue is how much the physical properties are affected by the octupolar interaction in comparison with the dipolar interaction.

4.2 *Temperature-dependent helical magnetic structure*

As shown in Fig. 7, the propagation vector changes with temperature by an amount proportional to the magnitude of the ordered moment. This suggests that the RKKY exchange interaction itself changes with the evolution of the ordered moment.[52)] The magnetic propagation vector generally reflects the $\boldsymbol{q}$ vector where the exchange interaction $J(\boldsymbol{q})$, the Fourier transform of J_{ij}, takes a maximum. $J(\boldsymbol{q})$ for the RKKY interaction is associated with the local c-f exchange interaction and $\chi(\boldsymbol{q})$ for the conduction electron system. Unfortunately, little is known yet about the Fermi surface of $Yb(Ni_{1-x}Cu_x)_3Al_9$. When a helimagnetic order develops on the Yb sites, a perturbation of the exchange field to the conduction electron system arises, which is also described by the same $\boldsymbol{q}$ vector. As a result, a gap appears in the region of the Fermi surface where $\varepsilon_{\boldsymbol{k}'} = \varepsilon_{\boldsymbol{k}+\boldsymbol{q}}$ is satisfied.[53)] This gap slightly modifies $\chi(\boldsymbol{q})$ and $J(\boldsymbol{q})$, resulting in a shift of the $\boldsymbol{q}$ vector.[54)] The $\boldsymbol{q}$-shift from the original value of $\boldsymbol{q}_0$ just below T_N becomes almost proportional to the ordered moment. A similar T dependence of the $\boldsymbol{q}$ vector has also been reported for GdSi, $GdNi_2B_2C$, and $GdPd_2Al_3$.[55–58)] In any case, concerning the most noteworthy phenomenon that the direction of the $\boldsymbol{q}$-shift differs below and above x=0.03, we have no explanation yet. Knowledge of the band structure and the Fermi surface is required.

If there were magnetic anisotropy, the T dependence of the $\boldsymbol{q}$ vector would be more complicated as observed in rare-earth metals.[52)] An anisotropy in the c plane would cause a squaring up and the appearance of the third-harmonic peak. This effect also causes the $\boldsymbol{q}$ vector to shift from $\boldsymbol{q}_0$. However, in such a case, the $\boldsymbol{q}$-shift becomes proportional to $(T_N - T)^2$, which is different from the present case of $Yb(Ni_{1-x}Cu_x)_3Al_9$.[52,59)] Furthermore, the $|7/2, \pm 1/2\rangle$ states in $Yb(Ni_{1-x}Cu_x)_3Al_9$ are almost isotropic in the c plane.

4.3 *Formation of chiral soliton lattice*

The results at zero field (Figs. 3 and 4) show that the helicity of the helimagnetic structure in $Yb(Ni_{1-x}Cu_x)_3Al_9$ has a one-to-one relation with the crystal chirality. This shows that a DM exchange interaction indeed exists, lifting the degeneracy between the left- and right-handed helical magnetic structures. The situation is similar to the well-investigated compound $CrNb_3S_6$, and $Yb(Ni_{1-x}Cu_x)_3Al_9$ can also be recognized as a monoaxial chiral helimagnet. The shift of the $\boldsymbol{q}$-vector and the appearance of the higher-harmonic peaks in magnetic fields (Figs. 8–10) suggest the formation of a CSL, a characteristic outcome of a monoaxial chiral helimagnet.

Theoretical study on the CSL state has been performed using the chiral sine-Gordon model, which has been successfully applied to $CrNb_3S_6$.[10)] For $CrNb_3S_6$, the application of the sine-Gordon model, where continuous variables are introduced to treat the spin arrangement, is justified because the modulation length of the helimagnetic structure L_0 ($\sim$ 480 Å) is much larger than the interlayer distance c_0 =12.1 Å. On the other hand, in $Yb(Ni_{1-x}Cu_x)_3Al_9$, it should be remarked that the longest L_0 of 61 Å for x=0.06 is only 6.7 times larger than c_0=9.1 Å (=c/3), which questions the simple application of the continuous model. However, without an appropriate the-

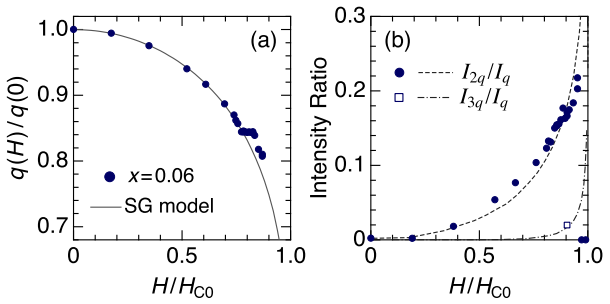

Fig. 15. (Color online) (a) Comparison of the experimental data of $q(H)/q(0)$ for $x = 0.06$ with the $L_0/L_{\rm CSL}$ curve obtained from the chiral sine-Gordon (SG) model.[10,11] $\mu_0 H_{C0}$ is set to 11.5 kG. (b) Comparison of the experimentally obtained intensity ratios of I_{2q}/I_q (filled circles) and I_{3q}/I_q (open square) with the calculated ratio for the sine-Gordon model using $\mu_0 H_{C0}$=10.5 kG.

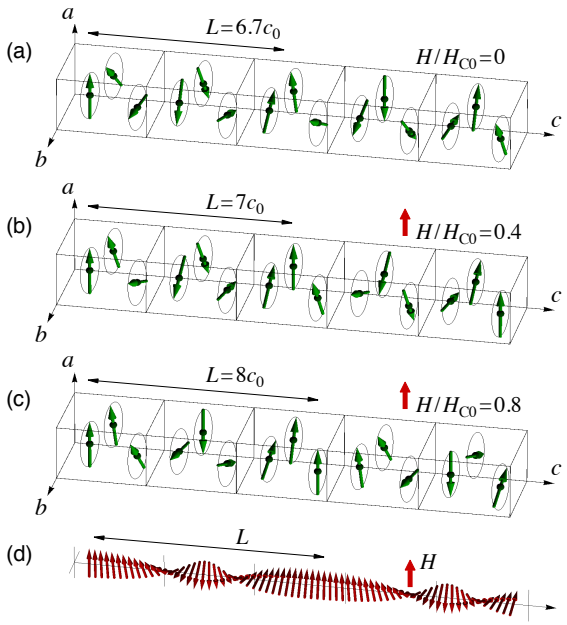

Fig. 16. (Color online) (a)–(c) Magnetic structures of $Yb(Ni_{1-x}Cu_x)_3Al_9$ for x=0.06 (L) in magnetic fields expected from the chiral sine-Gordon model. Only the moments on Yb-1 sites are shown. (a) Helimagnetic ordered state at zero field with q=0.445 and the helical pitch of L=6.7c_0. This is the same as Fig. 5. (b) CSL state for H/H_{C0}=0.4, corresponding to q=3/7 and L=7c_0 at around 5 kG. (c) CSL state for H/H_{C0}=0.8, corresponding to q=3/8 and L=8c_0 between 9.0 and 9.5 kG. (d) CSL state for continuous one-dimensional spin model corresponding to (c), H/H_{C0}=0.8.

ory at the present stage, it is worth comparing the results with the sine-Gordon model.

In Fig. 15(a), we compare the H dependence of the normalized propagation vector $q(H)/q(0)$ for $x = 0.06$ with the calculation of $L_0/L_{\rm CSL}$ for the sine-Gordon model.[10,11] We introduced a critical field of $\mu_0 H_{C0}$=11.5 kG so that the data fit the calculation. The data points closely follow the theoretical curve up to $H/H_{C0} \sim 0.85$, where the first-order transition to the ferromagnetic state takes place. In Fig. 15(b), we compare the intensity ratios of I_{2q}/I_q and I_{3q}/I_q with the theoretical curve by using a slightly different $\mu_0 H_{C0}$ of 10.5 kG. These intensity ratios also closely follow the theoretical curve. Although the calculation is for neutron diffraction, the result can almost equally be applied to the intensity of RXD. These agreements between the experiment and theory strongly indicate that the CSL state is actually formed in the $Yb(Ni_{1-x}Cu_x)_3Al_9$ system.

It is a problem, however, that the first-order transition at $H/H_{C0} \sim 0.85$ is not explained by the theory, probably because the sine-Gordon model is too simple to describe the actual magnetic exchange interactions in the $Yb(Ni_{1-x}Cu_x)_3Al_9$ system. It may be associated with the short period of the original helimagnetic structure. It is interesting to compare the $Yb(Ni_{1-x}Cu_x)_3Al_9$ system with the long-period system of $CrNb_3S_6$, in which the CSL state survives against the ferromagnetic state up to $H/H_{C0} \sim 0.97$.[12] Also, the lock-in phenomenon is not explained because the coupling with the lattice, other than the basal plane anisotropy, is not included in the theory. At the same time, we need to keep in mind why the continuous model of the sine-Gordon theory appears to be so applicable to the short-period system of $Yb(Ni_{1-x}Cu_x)_3Al_9$ below $H/H_{C0} \sim 0.85$. This is an important problem to be studied in future.

Putting aside the applicability of the theory, we show in Figs. 16(a)–16(c) the theoretically expected magnetic structures in magnetic fields for x=0.06 (L). Of special interest is the locked-in structure with q=3/8 between 9 and 9.5 kG, which is shown in Fig. 16(c). Another structure with q=3/7=0.4286, which is expected to appear at around 5 kG, is shown in Fig. 16(b) for comparison. Since it may be difficult to understand the CSL structure from these figures because of the discontinuity in the spin arrangement, we show for reference in Fig. 16(d) the CSL state for a continuous one-dimensional spin model corresponding to the CSL state in Fig. 16(c). The CSL structure in Fig. 16(c) gives rise to all the harmonics of q, $2q$, $3q$, $\cdots$. It also reproduces the $\Delta\theta_{\rm PR}$-scan data for the $2q$ peak shown in Fig. 12(b) because the structure factor is written in the same way as $(1, \pm i, 0)$. These consistencies with the data suggest that the CSL structure in Fig. 16(c) is actually realized. If this is the case, there should be no reason why the q=3/7 structure of Fig. 16(b) is not stabilized. Experimentally, however, the q=3/7 structure does not seem to be locked in at around 5 kG as observed in Fig. 9. This shows that the lock-in behavior is strongly associated with the CSL formation. The CSL with q=3/8 at 9 kG locks in the lattice because the CSL is well developed, whereas the CSL with q=3/7 is not locked in because it is still weak at 5 kG.

4.4 Magnetic exchange and DM interactions

There are many problems concerning the magnetic exchange and DM interactions in this system. The sine-Gordon theory is based on the following one-dimensional model for a layered monoaxial chiral helimagnet with ferromagnetic nearest-neighbor exchange and DM interaction:

$$\mathcal{H} = -J_1 \sum_i \boldsymbol{S}_i \cdot \boldsymbol{S}_{i+1} - \boldsymbol{D} \cdot \sum_i \boldsymbol{S}_i \times \boldsymbol{S}_{i+1} - \sum_i \boldsymbol{S}_i \cdot \boldsymbol{H}, \quad (9)$$

where $\boldsymbol{S}_i$ lies in the xy plane, $\boldsymbol{D}$ is along the z axis, and $\boldsymbol{H}$ is applied in the xy plane. At $H = 0$, a helimagnetic order with $q_0 = c_0^{-1} \arctan(D/J_1)$ is formed, where c_0 is the interlayer distance. If we simply apply this model to $Yb(Ni_{1-x}Cu_x)_3Al_9$ to obtain q_0 values of 0.42, 0.54, and 0.63 for x=0.06, 0.04, and 0.02, D/J_1 is required to be 1.2, 2.1, and 3.9, respectively,

which are unrealistically large. For x=0, in addition, it is impossible to reproduce q_0=0.82 from this model because the angle between spins on neighboring layers is larger than 90°. To explain these large q_0 values, it is necessary to include more long-range exchange interactions mediated by the conduction electrons. It is more reasonable to consider that q_0 is determined mainly by J_1 (> 0), J_2 (< 0), and further interactions, with which $J(q)$ takes a maximum at q_0. If we consider J_1 and J_2, for example, $J(q) = J_1 \cos qc_0 + J_2 \cos 2qc_0$, and q_0 is given by $c_0^{-1} \arccos(-J_1/4J_2)$. The degeneracy of $\pm q_0$ is lifted by the DM term.

However, there still remains a problem. If q_0 is determined by the maximum of $J(q)$, it is expected that $T_N \propto J(q_0)$ and $H_C \propto J(q_0) - J(0)$. When q_0 approaches 0 (ferromagnetic state) with increasing Cu concentration, $J(q_0) - J(0)$ should also become small because $J(q)$ is a symmetric function of q.[60] However, while T_N=6.5 K for x=0.06 is twice as large as that for x =0, $\mu_0 H_C$=10 kG for x=0.06 is ten times as large as that for x=0. These facts are not explained by the simplistic model above and show that the situation behind the helimagnetic order of $Yb(Ni_{1-x}Cu_x)_3Al_9$ is not so simple. Firstly, the interaction between Yb-1 and Yb-2 moments should be considered. More importantly, the fact that H_C significantly increases with increasing x, i.e., with decreasing q_0 and $J(q_0) - J(0)$, suggests that the nonlinear effect of the CSL formation in magnetic fields plays an important role in keeping the helimagnetic structure and preventing the system from undergoing a transition to the ferromagnetic state. The possibility of the DM interaction increasing with increasing Cu concentration should also be considered.

5. Summary

We performed resonant X-ray diffraction experiments to investigate the helical magnetic structure of $Yb(Ni_{1-x}Cu_x)_3Al_9$ with the space group $R32$, which lacks both inversion and mirror symmetries and allows the existence of left- and right-handed crystal structures.

- We showed that the magnetic structure is described by an incommensurate propagation vector $(0, 0, q)$, where q=0.818, 0.617, 0.553, and 0.445 for x=0, 0.02, 0.04, and 0.06, respectively, at the lowest temperature. The magnetic moments lie in the c plane.
- We clarified that the helicity of the magnetic structure has a one-to-one relation with the crystal chirality, indicating that an antisymmetric exchange interaction mediated by the conduction electrons exists, i.e., the RKKY mechanism. A theoretical study is required to provide further insight into the physical mechanism.
- When a magnetic field is applied perpendicular to the helical axis, the q value decreases (the helical pitch increases) and, simultaneously, the higher-harmonic peaks of $2q$ and $3q$ are induced with increasing field. This behavior, especially for the x=0.06 case, coincides with the calculation for the chiral sine-Gordon model, which describes the formation of the chiral soliton lattice (CSL) state in a monoaxial helimagnet. This coincidence provides strong evidence for the CSL formation in $Yb(Ni_{1-x}Cu_x)_3Al_9$, which has been suggested by magnetization measurement. However, since the helical pitch is not much longer than the interlayer spacing, it is questionable if the spin arrangement could be approximated as a continuous medium. The applicability of the sine-Gordon model to $Yb(Ni_{1-x}Cu_x)_3Al_9$ remains a question. The lock-in phenomenon at $q = 3/8$ and the first-order transition to the ferromagnetic state also are important issues to be studied.
- We observed an anomalous temperature dependence of the propagation vector. The q value changes with temperature by an amount almost in proportion to the magnetic order parameter, which we ascribed to the change in the exchange interaction with the development of the ordered moment. It is not understood, however, why the q value decreases with decreasing T for $x < 0.03$, but this is reversed for $x > 0.03$.
- The helical ordering of the magnetic octupole moment was detected, which arises simultaneously with the helical ordering of the magnetic dipole moment, reflecting the anisotropic charge density of the crystal field ground state of Yb^{3+}, consisting mainly of $|7/2, \pm 1/2\rangle$.

Acknowledgements

We acknowledge valuable comments by H. Ohsumi, M. Suzuki, T. Nagao, R. Shiina, A. Leonov, and J. Kishine. This work was supported by JSPS KAKENHI Grant Numbers 15K05175, 26400333, 16H01073, 15H05885, 17H02912, and 16KK0102. The synchrotron radiation experiment was performed under Proposals No. 2015B3711, No. 2016A3761, No. 2016B3762, and No. 2017A3787 at BL22XU of SPring-8. We also acknowledge support by the JSPS Core-to-Core Program, A. Advanced Research Networks. Magnetization measurement with the MPMS and the electron probe microanalysis were performed at N-BARD, Hiroshima University.

Appendix A: Confirmation of the Crystal Structure

A.1 Crystal chirality

The crystal chirality of the sample, especially the spot where the X-ray beam is irradiated in the RXD experiment, can be confirmed at the beamline by measuring the energy dependence of an appropriate fundamental Bragg peak as shown in Fig. A·1. The structure factor of the $(1, 1, 24)$ fundamental reflection for the right-handed crystal is expressed as $F_{R,(1,1,24)}(\omega) = A_{Al} f_{Al}(\omega) + A_{Ni} f_{Ni}(\omega) + A_{Yb} f_{Yb}(\omega)$, where $A_{Al} = 0.24 + 24.6i$, $A_{Ni} = -8.6 + 14.9i$, and $A_{Yb} = 6.0$. $F_{L,(\bar{1},\bar{1},24)}$ also has the same expression. For $F_{L,(1,1,24)}$ and $F_{R,(\bar{1},\bar{1},24)}$, we take the complex conjugates for A_{Al} and A_{Ni}. When $f_{Yb}(\omega) = f_{0,Yb} + f'_{Yb}(\omega) + if''_{Yb}(\omega)$ exhibits an anomalous dispersion around the absorption edge, the intensity of the Bragg reflection also exhibits a strong energy dependence. Since the intensities for the right- and left-handed crystals are expressed as $|F_{R,(1,1,24)}(\omega)|^2$ and $|F_{L,(1,1,24)}(\omega)|^2$, respectively, they exhibit different energy dependences due to the different interference effect. As shown in Fig. A·1, the relative relation of the intensity is reversed for the $(\bar{1}, \bar{1}, 24)$ reflection. The relationship of the intensity is consistent with the calculated spectrum assuming the predetermined crystal chirality.

A.2 Threefold symmetry about the c axis

Figure A·2 shows the rocking scans of the $(1, 0, L)$ reflections for the x=0.06 (L) sample. Only the $(1, 0, 3n + 1)$ reflection is allowed in the $(1, 0, L)$ reflections in the $R32$ space group. These data guarantee the threefold symmetry of this

sample about the c axis. If the forbidden reflection is observed, it means that the [1 1 0] axis is mixed with the a axis due to the stacking fault of 60°.

Appendix B: Formalism of Resonant X-ray Scattering

We use the scattering-amplitude-operator method to analyze the experimental results.[42] We consider a 2×2 matrix $\hat{F}$, consisting of four elements of the scattering amplitudes for σ-σ', π-σ', σ-π', and π-π':

$$\hat{F} = \begin{pmatrix} F_{\sigma\sigma'} & F_{\pi\sigma'} \\ F_{\sigma\pi'} & F_{\pi\pi'} \end{pmatrix}. \tag{B·1}$$

By using the identity matrix $\hat{I}$ and the Pauli matrix $\hat{\boldsymbol{\sigma}}$, $\hat{F}$ can generally be expressed as

$$\hat{F} = \beta\hat{I} + \boldsymbol{\alpha}\cdot\hat{\boldsymbol{\sigma}} = \begin{pmatrix} \beta+\alpha_3 & \alpha_1 - i\alpha_2 \\ \alpha_1 + i\alpha_2 & \beta-\alpha_3 \end{pmatrix}. \tag{B·2}$$

Once we know the matrix $\hat{F}$, the scattering cross section $(d\sigma/d\Omega)$ can be calculated by

$$\begin{aligned}\left(\frac{d\sigma}{d\Omega}\right) &= \mathrm{Tr}\{\hat{\mu}\hat{F}^*\hat{F}\} \\ &= \beta^*\beta + \boldsymbol{\alpha}^*\cdot\boldsymbol{\alpha} + \beta^*(\boldsymbol{P}\cdot\boldsymbol{\alpha}) + (\boldsymbol{P}\cdot\boldsymbol{\alpha}^*)\beta \\ &\quad + i\boldsymbol{P}\cdot(\boldsymbol{\alpha}^*\times\boldsymbol{\alpha}),\end{aligned} \tag{B·3}$$

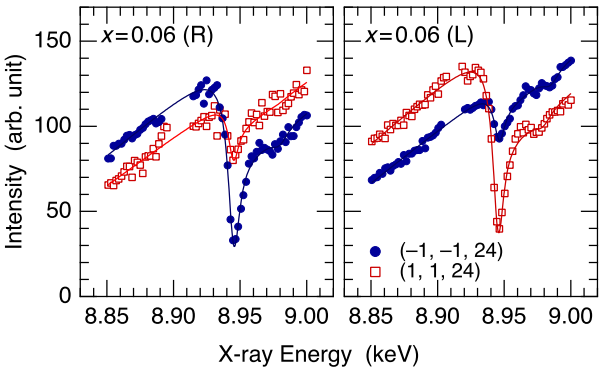

Fig. A·1. (Color online) X-ray energy dependence of the $(1,1,24)$ and $(\bar{1},\bar{1},24)$ fundamental reflections for the right- and left-handed crystals for x=0.06 around the L_3 absorption edge of Yb. Solid lines are the guides for the eye.

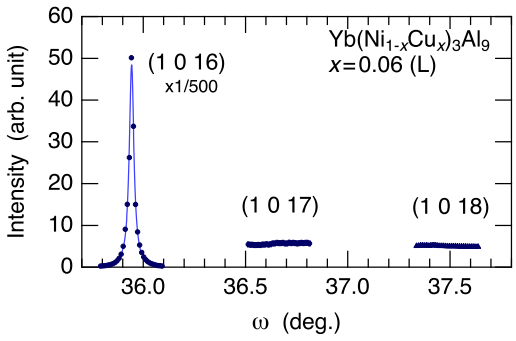

Fig. A·2. (Color online) Rocking scans of the $(1,0,16)$, $(1,0,17)$, and $(1,0,18)$ reflections for the x=0.06 (L) sample.

where $\hat{\mu} = (\hat{I} + \boldsymbol{P}\cdot\hat{\boldsymbol{\sigma}})/2$ represents the density matrix and the Stokes vector $\boldsymbol{P} = (P_1, P_2, P_3)$ represents the polarization state of the incident photon. P_1, P_2, and P_3 represent the degrees of +45° ($P_1 = 1$) or −45° ($P_1 = -1$) linear polarization, right ($P_2 = 1$) or left ($P_2 = -1$)-handed circular polarization, and the σ ($P_3 = 1$) or π ($P_3 = -1$) linear polarization state, respectively.

Using the elements of Eq. (B·1), the scattering cross section is expressed as

$$\begin{aligned}\left(\frac{d\sigma}{d\Omega}\right) &= \frac{1}{2}\left(|F_{\sigma\sigma'}|^2 + |F_{\sigma\pi'}|^2 + |F_{\pi\sigma'}|^2 + |F_{\pi\pi'}|^2\right) \\ &\quad + P_1\mathrm{Re}\{F^*_{\pi\sigma'}F_{\sigma\sigma'} + F^*_{\pi\pi'}F_{\sigma\pi'}\} \\ &\quad + P_2\mathrm{Im}\{F^*_{\pi\sigma'}F_{\sigma\sigma'} + F^*_{\pi\pi'}F_{\sigma\pi'}\} \\ &\quad + \frac{1}{2}P_3\left(|F_{\sigma\sigma'}|^2 + |F_{\sigma\pi'}|^2 - |F_{\pi\sigma'}|^2 - |F_{\pi\pi'}|^2\right).\end{aligned} \tag{B·4}$$

Therefore, the cross section for the incident beam described by (P_1, P_2, P_3) can generally be written as

$$\left(\frac{d\sigma}{d\Omega}\right) = C_0 + C_1P_1 + C_2P_2 + C_3P_3, \tag{B·5}$$

which can be used as a fitting function for the $\Delta\theta_{\mathrm{PR}}$ scan with the four parameters of C_n ($n = 0 \sim 3$).

The four elements of Eq. (B·1) at an X-ray energy $E = \hbar\omega$ near the resonance energy are expressed as

$$F_{\varepsilon\varepsilon'} = F_{E1,\varepsilon\varepsilon'}(\omega) + F_{E2,\varepsilon\varepsilon'}(\omega). \tag{B·6}$$

$F_{E1,\varepsilon\varepsilon'}(\omega)$ and $F_{E2,\varepsilon\varepsilon'}(\omega)$ for a scattering process from the photon state $(\boldsymbol{\varepsilon}, \boldsymbol{k})$ to $(\boldsymbol{\varepsilon}', \boldsymbol{k}')$ are expressed as

$$F_{E1,\varepsilon\varepsilon'}(\omega) = \sum_{\nu=0}^{2}\alpha^{(\nu)}_{E1}(\omega)\sum_{\Gamma}\boldsymbol{X}^{(\nu)}_{E1,\Gamma}(\boldsymbol{\varepsilon},\boldsymbol{\varepsilon}')\cdot\langle\boldsymbol{Z}^{(\nu)}_{\Gamma}\rangle, \tag{B·7}$$

$$F_{E2,\varepsilon\varepsilon'}(\omega) = \sum_{\nu=0}^{4}\alpha^{(\nu)}_{E2}(\omega)\sum_{\Gamma}\boldsymbol{X}^{(\nu)}_{E2,\Gamma}(\boldsymbol{\varepsilon},\boldsymbol{\varepsilon}',\hat{\boldsymbol{k}},\hat{\boldsymbol{k}}')\cdot\langle\boldsymbol{Z}^{(\nu)}_{\Gamma}\rangle. \tag{B·8}$$

$\langle\boldsymbol{Z}^{(\nu)}_{\Gamma}\rangle$ represents the structure factor of the rank-ν multipole moment of the irreducible representation Γ in the cubic coordinates. $\boldsymbol{X}^{(\nu)}_{\Gamma}$ is the geometrical factor corresponding to $\langle\boldsymbol{Z}^{(\nu)}_{\Gamma}\rangle$. For the rank-1 dipole moment with the T_{1u} representation,

$$\boldsymbol{X}^{(1)}_{E1,\mathrm{dip}} = \frac{i}{\sqrt{2}}(\boldsymbol{\varepsilon}'\times\boldsymbol{\varepsilon}), \tag{B·9}$$

$$\begin{aligned}\boldsymbol{X}^{(1)}_{E2,\mathrm{dip}} &= \frac{i}{2\sqrt{10}}\{(\boldsymbol{k}'\cdot\boldsymbol{k})(\boldsymbol{\varepsilon}'\times\boldsymbol{\varepsilon}) + (\boldsymbol{\varepsilon}'\cdot\boldsymbol{\varepsilon})(\boldsymbol{k}'\times\boldsymbol{k}) \\ &\quad + (\boldsymbol{k}'\cdot\boldsymbol{\varepsilon})(\boldsymbol{\varepsilon}'\times\boldsymbol{k}) + (\boldsymbol{\varepsilon}'\cdot\boldsymbol{k})(\boldsymbol{k}'\times\boldsymbol{\varepsilon})\}.\end{aligned} \tag{B·10}$$

See Ref. 36 for $\boldsymbol{X}^{(3)}_{E2}$. The scattering amplitude is obtained by taking the scalar product of $\boldsymbol{X}^{(\nu)}_{\Gamma}$ and $\langle\boldsymbol{Z}^{(\nu)}_{\Gamma}\rangle$.

The same result is obtained by using the spherical tensor method.[35] By transforming $\langle\boldsymbol{Z}^{(\nu)}_{\Gamma}\rangle$ in the cubic representation to $\langle T^{(\nu)}_q\rangle$ in the spherical representation,

$$F_{E1,\varepsilon\varepsilon'}(\omega) = \sum_{\nu=0}^{2}\alpha^{(\nu)}_{E1}(\omega)\sum_{q=-\nu}^{\nu}(-1)^q X^{(\nu)}_{E1,-q}\langle T^{(\nu)}_q\rangle, \tag{B·11}$$

$$F_{E2,\varepsilon\varepsilon'}(\omega) = \sum_{\nu=0}^{4} \alpha_{E2}^{(\nu)}(\omega) \sum_{q=-\nu}^{\nu} (-1)^q X_{E2,-q}^{(\nu)} \langle T_q^{(\nu)} \rangle \,, \qquad \text{(B·12)}$$

where the geometrical factors of $X_{E1,q}^{(\nu)}$ and $X_{E2,q}^{(\nu)}$ are also expressed in the spherical representation as

$$X_{E1,q}^{(\nu)} = \sum_{p,p'=-1}^{1} \varepsilon'_p \varepsilon_{p'} \langle 1p1p'|\nu q\rangle \,, \qquad \text{(B·13)}$$

$$X_{E2,q}^{(\nu)} = \sum_{p,p'=-2}^{2} h'_{p'} h_p \langle 2p2p'|\nu q\rangle \,, \qquad \text{(B·14)}$$

$$h_m = \sum_{p,p'=-1}^{1} \varepsilon_p k_{p'} \langle 1p1p'|2m\rangle \,, \qquad \text{(B·15)}$$

$$h'_m = \sum_{p,p'=-1}^{1} \varepsilon'_p k'_{p'} \langle 1p1p'|2m\rangle \,. \qquad \text{(B·16)}$$

It is important that the spectral functions of $\alpha_{E1}^{(\nu)}(\omega)$ and $\alpha_{E2}^{(\nu)}(\omega)$ are rank-dependent.[36,37] In the data analysis, each of them may be approximated by the form

$$\alpha^{(\nu)}(\omega) = \frac{e^{i\phi_\nu}}{\hbar\omega - \Delta + i\gamma} \,, \qquad \text{(B·17)}$$

where Δ, γ, and ϕ_ν are the resonance energy, lifetime broadening effect, and phase factor, respectively.

1) G. H. Wagniére, *On Chirality and the Universal Asymmetry* (VHCA, Zürich & Wiley-VCH, Weinheim, 2007).
2) I. Dzyaloshinsky, J. Phys. Chem. Solids **4**, 241 (1958).
3) T. Moriya, Phys. Rev. **120**, 91 (1960).
4) H. Katsura, N. Nagaosa, and A. V. Balatsky, Phys. Rev. Lett. **95**, 057205 (2005).
5) X. Z. Yu, Y. Onose, N. Kanazawa, J. H. Park, J. H. Han, Y. Matsui, N. Nagaosa, and Y. Tokura, Nature **465**, 901 (2010).
6) X. Z. Yu, N. Kanazawa, Y. Onose, K. Kimoto, W. Z. Zhang, S. Ishiwata, Y. Matsui, and Y. Tokura, Nat. Mater. **10**, 106 (2010).
7) D. McGrouther, R. J. Lamb, M. Krajnak, S. McFadzean, S. McVitie, R. L. Stamps, A. O. Leonov, A. N. Bogdanov, and Y. Togawa, New J. Phys. **18**, 095004 (2016).
8) S. Seki, X. Z. Yu, S. Ishiwata, and Y. Tokura, Science **336**, 198 (2012).
9) A. O. Leonov, Y. Togawa, T. L. Monchesky, A. N. Bogdanov, J. Kishine, Y. Kousaka, M. Miyagawa, T. Koyama, J. Akimitsu, T. Koyama, K. Harada, S. Mori, D. McGrouther, R. Lamb, M. Krajnak, S. McVitie, R. L. Stamps, and K. Inoue, Phys. Rev. Lett. **117**, 087202 (2016).
10) J. Kishine and A. S. Ovchinnikov, Solid State Phys. **66**, 1 (2015).
11) Y. Togawa, Y. Kousaka, K. Inoue, and J. Kishine, J. Phys. Soc. Jpn. **85**, 112001 (2016).
12) Y. Togawa, T. Koyama, K. Takayanagi, S. Mori, Y. Kousaka, J. Akimitsu, S. Nishihara, K. Inoue, A. S. Ovchinnikov, and J. Kishine, Phys. Rev. Lett. **108**, 107202 (2012).
13) Y. Togawa, Y. Kousaka, S. Nishihara, K. Inoue, J. Akimitsu, A. S. Ovchinnikov, and J. Kishine, Phys. Rev. Lett. **111**, 197204 (2013).
14) Y. Togawa, T. Koyama, Y. Nishimori, Y. Matsumoto, S. McVitie, D. McGrouther, R. L. Stamps, Y. Kousaka, J. Akimitsu, S. Nishihara, K. Inoue, I. G. Bostrem, V. E. Sinitsyn, A. S. Ovchinnikov, and J. Kishine, Phys. Rev. B **92**, 220412 (2015).
15) K. Tsuruta, M. Mito, Y. Kousaka, J. Akimitsu, J. Kishine, Y. Togawa, H. Ohsumi, and K. Inoue, J. Phys. Soc. Jpn. **85**, 013707 (2016).
16) L. Wang, N. Chepiga, D.-K. Ki, L. Li, W. Zhu, Y. Kato, O. S. Ovchinnikova, F. Mila, I. Martin, D. Mandrus, and A. F. Morpurgo, Phys. Rev. Lett. **118**, 257203 (2017).
17) R. E. Gladyshevskii, Acta Crystallogr. B **49**, 468 (1993).
18) P. H. Tobash, Y. Jiang, F. Ronning, C. H. Booth, J. D. Thompson, B. L. Scott, and E. D. Bauer, J. Phys.: Condens. Matter **23**, 086002 (2011).
19) K. Momma and F. Izumi, J. Appl. Crystallogr. **44**, 1272 (2011).
20) S. Ohara, T. Yamashita, Y. Mori, and I. Sakamoto, J. Phys.: Conf. Ser. **273**, 012048 (2011).
21) T. Yamashita, S. Ohara, and I. Sakamoto, J. Phys. Soc. Jpn. **80**, SA080 (2011).
22) T. Yamashita, R. Miyazaki, Y. Aoki, and S. Ohara, J. Phys. Soc. Jpn. **81**, 034705 (2012).
23) R. Miyazaki, Y. Aoki, R. Higashinaka, H. Sato, T. Yamashita, and S. Ohara, Phys. Rev. B **86**, 155106 (2012).
24) T. Hirayama, K. Matsubayashi, T. Yamashita, S. Ohara, K. Munakata, and Y. Uwatoko, J. Phys.: Conf. Ser. **391**, 012020 (2012).
25) Y. Utsumi, H. Sato, S. Ohara, T. Yamashita, K. Mimura, S. Motonami, K. Shimada, S. Ueda, K. Kobayashi, H. Yamaoka, N. Tsujii, N. Hiraoka, H. Namatame, and M. Taniguchi, Phys. Rev. B **86**, 115114 (2012).
26) S. Ohara, S. Fukuta, K. Ohta, H. Kono, T. Yamashita, Y. Matsumoto, and J. Yamaura, JPS Conf. Proc. **3**, 017016 (2014).
27) T. Miyadai, K. Kikuchi, H. Kondo, S. Sakka, M. Arai, and Y. Ishikawa, J. Phys. Soc. Jpn. **52**, 1394 (1983).
28) M. Ishida, Y. Endoh, S. Mitsuda, Y. Ishikawa, and M. Tanaka, J. Phys. Soc. Jpn. **54**, 2975 (1985).
29) Y. Yamasaki, H. Sagayama, T. Goto, M. Matsuura, K. Hirota, T. Arima, and Y. Tokura, Phys. Rev. Lett. **98**, 147204 (2007).
30) C. Sutter, G. Grübel, C. Vettier, F. de Bergevin, A. Stunault, D. Gibbs, and C. Giles, Phys. Rev. B **55**, 954 (1997).
31) F. Fabrizi, H. C. Walker, L. Paolasini, F. de Bergevin, A. T. Boothroyd, D. Prabhakaran, and D. F. McMorrow, Phys. Rev. Lett. **102**, 237205 (2009).
32) H. Sagayama, N. Abe, K. Taniguchi, T. Arima, Y. Yamasaki, D. Okuyama, Y. Tokura, S. Sakai, T. Morita, T. Komesu, H. Ohsumi, and M. Takata, J. Phys. Soc. Jpn. **79**, 043711 (2010).
33) J. P. Hannon, G. T. Trammell, M. Blume, and D. Gibbs, Phys. Rev. Lett. **62**, 2644 (1988) [Errata **62**, 2644 (1988)].
34) Y. Yamasaki, D. Morikawa, T. Honda, H. Nakao, Y. Murakami, N. Kanazawa, M. Kawasaki, T. Arima, and Y. Tokura, Phys. Rev. B **92**, 220421 (2015).
35) S. W. Lovesey, E. Balcar, K. S. Knight, and J. Fernández-Rodríguez, Phys. Rep. **411**, 233 (2005).
36) T. Nagao and J. I. Igarashi, Phys. Rev. B **74**, 104404 (2006).
37) T. Nagao and J. Igarashi, Phys. Rev. B **82**, 024402 (2010).
38) Y. Kousaka, H. Ohsumi, T. Komesu, T. Arima, M. Takata, S. Sakai, M. Akita, K. Inoue, T. Yokobori, Y. Nakao, E. Kaya, and J. Akimitsu, J. Phys. Soc. Jpn. **78**, 123601 (2009).
39) Y. Tanaka, T. Takeuchi, S. W. Lovesey, K. S. Knight, A. Chainani, Y. Takata, M. Oura, Y. Senba, H. Ohashi, and S. Shin, Phys. Rev. Lett. **100**, 145502 (2012) [Errata **108**, 019901 (2012)].
40) Y. Tanaka and S. W. Lovesey, Eur. Phys. J. Spec. Top. **208**, 67 (2012).
41) T. Inami, S. Michimura, and T. Matsumura, J. Phys.: Conf. Ser. **425**, 132011 (2013).
42) S. W. Lovesey and S. P. Collins, *X-ray Scattering and Absorption by Magnetic Materials* (Oxford, New York, 1996).
43) K. Munakata, Y. Nambu, T. Tanaka, K. Matsubayashi, T. Hirayama, T. Yamashita, S. Ohara, and Y. Uwatoko, private communication.
44) S. Ohara, private communication.
45) (Supplemental material) The results of the disagreeing calculations are provided online in Fig. S1.
46) (Supplemental material) The irreducible representation in the D_3 point group is provided online in Table S1.
47) H. Kusunose, J. Phys. Soc. Jpn. **77**, 064710 (2008).
48) R. Shiina, H. Shiba, and P. Thalmeier, J. Phys. Soc. Jpn. **66**, 1741 (1997).
49) H. Shiba, O. Sakai, and R. Shiina, J. Phys. Soc. Jpn. **68**, 1988 (1999).
50) T. Matsumura, T. Yonemura, K. Kunimori, M. Sera, F. Iga, T. Nagao, and J. I. Igarashi, Phys. Rev. B **85**, 174417 (2012).
51) T. Matsumura, S. Michimura, T. Inami, T. Otsubo, H. Tanida, F. Iga, and M. Sera, Phys. Rev. B **89**, 014422 (2014).
52) J. Jensen and A. R. Mackintosh, *Rare Earth Magnetism* (Clarendon Press, Oxford, 1991).
53) R. E. Watson, A. J. Freeman, and J. P. Dimmock, Phys. Rev. **167**, 497 (1968).
54) R. J. Elliot and F. A. Wedgwood, Proc. Phys. Soc. **84**, 63 (1964).
55) Y. Feng, J. Wang, D. M. Silevitch, B. Mihaila, J. W. Kim, J.-Q. Yan, R. K. Schulze, N. Woo, A. Palmer, Y. Ren, J. van Wezel, P. B. Littlewood, and T. F. Rosenbaum, Proc. Nat. Acad. Sci. U.S.A. **110**, 3287 (2013).
56) Y. Feng, D. M. Silevitch, J. Wang, A. Palmer, N. Woo, J.-Q. Yan, Z.

Islam, A. V. Suslov, P. B. Littlewood, and T. F. Resenbaum, Phys. Rev. B **88**, 134404 (2013).
57) C. Detlefs, A. I. Goldman, C. Stassis, P. C. Canfield, B. K. Cho, J. P. Hill, and D. Gibbs, Phys. Rev. B **53**, 6355 (1996).
58) T. Inami, N. Terada, H. Kitazawa, and O. Sakai, J. Phys. Soc. Jpn. **78**, 084713 (2009).
59) T. Sato, H. Kadowaki, H. Masuda, and K. Iio, J. Phys. Soc. Jpn. **63**, 4583 (1994).
60) (Supplemental material) A simple calculation assuming J_1 and J_2 is provided online in Fig. S2.

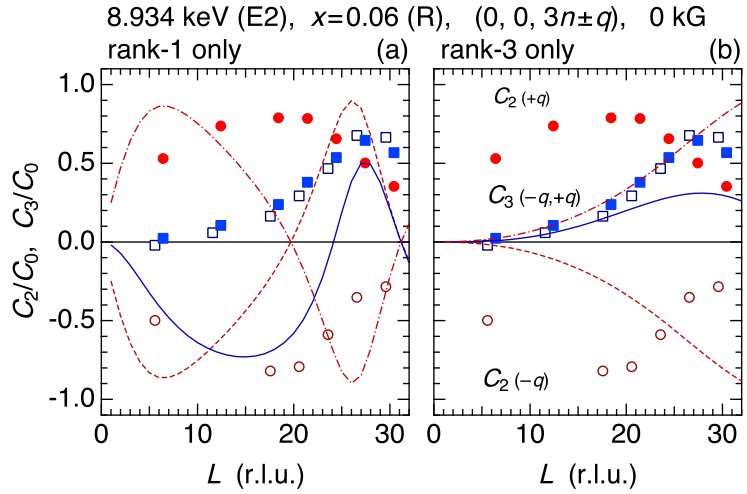

Fig. S·1. Comparison of the disagreeing calculation with the L (= $3n \pm q$) dependence data of the parameters C_2/C_0 and C_3/C_0 at zero field, which was obtained from the $\Delta\theta_{PR}$ scans for the x=0.06 (R) sample at the $E2$ resonance energy. Solid, dashed, and dot-dashed curves represent the calculation of C_3/C_0 ($L = 3n \pm q$), C_2/C_0 ($L = 3n - q$), and C_2/C_0 ($L = 3n + q$), respectively, for models of (a) $\langle J_x \pm iJ_y \rangle$ dipole (rank-1) only and (b) $\langle T^\gamma_x \pm iT^\gamma_y \rangle$ octupole (rank-3) only. The data can be explained by mixing these two scattering contributions as described in the main text.

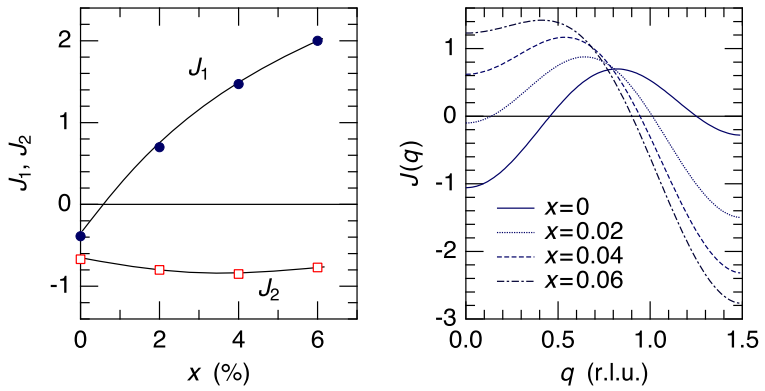

Fig. S·2. A simple calculation of $J(q)$ for one dimensional spin chain with nearest-neighbor exchange J_1 and next-nearest-neighbor exchange J_2. J_1 and J_2 are taken so that $q_0 = c_0^{-1} \arccos(-J_1/4J_2)$, where $J(q) = J_1 \cos qc_0 + J_2 \cos 2qc_0$ takes the maximum, reproduces the experimental value and $J(q_0)$ is proportional to T_N. The degeneracy at $\pm q_0$ will be lifted by including the DM term. In this model, without considering any nonlinear effect such as CSL formation, H_C will be proportional to $J(q_0) - J(0)$. However, it is contradictory to the experimental result.

Table S·1. Irreducible representation (Irrep.), operator notation, and basis functions of the dipole (rank-1) and octupole (rank-3) moments in the O_h and D_3 point groups.

	O_h			D_3		
Rank	Irrep.	Notation	Basis Function	Irrep.	Notation	Basis Function
1	T_{1u}	J_x	x	E_u	J_x	x
		J_y	y		J_y	y
		J_z	z	A_{2u}	J_z	z
3	T_{1u}	T^α_x	$x(5x^2 - 3r^2)/2$	E_u	$T^\gamma_x = (-\sqrt{3}T^\alpha_x - \sqrt{5}T^\beta_x)/2\sqrt{2}$	$\sqrt{6}x(5z^2 - r^2)/4$
		T^α_y	$y(5y^2 - 3r^2)/2$		$T^\gamma_y = (-\sqrt{3}T^\alpha_y + \sqrt{5}T^\beta_y)/2\sqrt{2}$	$\sqrt{6}y(5z^2 - r^2)/4$
		T^α_z	$z(5z^2 - 3r^2)/2$	A_{2u}	T^α_z	$z(5z^2 - 3r^2)/2$
	T_{2u}	T^β_x	$\sqrt{15}x(y^2 - z^2)/2$	A_{2u}	$T^\delta_x = (\sqrt{5}T^\alpha_x - \sqrt{3}T^\beta_x)/2\sqrt{2}$	$\sqrt{10}x(x^2 - 3y^2)/4$
		T^β_y	$\sqrt{15}y(z^2 - x^2)/2$	A_{1u}	$T^\delta_y = (\sqrt{5}T^\alpha_y + \sqrt{3}T^\beta_y)/2\sqrt{2}$	$\sqrt{10}y(y^2 - 3x^2)/4$
		T^β_z	$\sqrt{15}z(x^2 - y^2)/2$	E_u	T^β_z	$\sqrt{15}z(x^2 - y^2)/2$
	A_{2u}	T_{xyz}	$\sqrt{15}xyz$		T_{xyz}	$\sqrt{15}xyz$